PAPER

A combined crystallographic and theoretical investigation of noncovalent interactions in 1,3,4-oxadiazole-2-thione-*N*-Mannich derivatives: *in vitro* bioactivity and molecular docking†

Lamya H. Al-Wahaibi, [ID] [a] Kowsalya Alagappan,[b] Rosa M. Gomila, [ID] [c] Olivier Blacque, [ID] [d] Antonio Frontera, [ID] *[c] M. Judith Percino, [ID] [e] Ali A. El-Emam [ID] *[f] and Subbiah Thamotharan [ID] *[b]

Two 1,3,4-oxadiazole-2-thione-*N*-Mannich derivatives, specifically 5-(4-chlorophenyl)-3-[(2-trifluoromethylphenylamino)methyl]-1,3,4-oxadiazole-2(3*H*)-thione (**1**) and 5-(4-chlorophenyl)-3-[(2,5-difluorophenylamino)methyl]-1,3,4-oxadiazole-2(3*H*)-thione (**2**), were synthesized and then characterized by elemental analysis and NMR (^{1}H and ^{13}C) spectroscopy and the single crystal X-ray diffraction method. The formed weak intermolecular interactions in the solid-state structures of these derivatives were thoroughly investigated utilizing a variety of theoretical tools such as Hirshfeld surface analysis and quantum theory of atoms in molecules (QTAIM). Furthermore, the CLP-PIXEL and density functional theory calculations were used to study the energetics of molecular dimers. Numerous weak intermolecular interactions such as C–H···S/Cl/F/π interactions, a directional C–Cl···Cl halogen bond, π-stacking, type C–F···F–C contact and a short F···O interaction, help to stabilize the crystal structure of **1**. Crystal structure **2** also stabilizes with several weak intermolecular contacts, including N–H···S, C–H···N//Cl/F interactions, a highly directional C1–Cl1···C(π) halogen bond and C(π)···C(π) interaction. *In vitro* antimicrobial potency of compounds **1** and **2** was assessed against various Gram-positive and Gram-negative bacterial strains and the pathogenic yeast-like *Candida albicans*. Both compounds showed marked activity against all tested Gram-positive bacteria and weak activity against *Escherichia coli* and lacked inhibitory activity against *Pseudomonas aeruginosa*. In addition, compounds **1** and **2** displayed good *in vitro* anti-proliferative activity against hepatocellular carcinoma (HepG-2) and mammary gland breast cancer (MCF-7) cancer cell lines. Molecular docking studies revealed the binding modes of title compounds at the active sites of prospective therapeutic targets.

aDepartment of Chemistry, College of Sciences, Princess Nourah bint Abdulrahman University, Riyadh 11671, Saudi Arabia

bBiomolecular Crystallography Laboratory and DBT-Bioinformatics Center, School of Chemical and Biotechnology, SASTRA Deemed University, Thanjavur 613 401, India. E-mail: thamu@scbt.sastra.edu

cDepartament de Química, Universitat de les Illes Balears, Ctra. de Valldemossa km 7.5, Baleares, 07122 Palma de Mallorca, Spain. E-mail: toni.frontera@uib.es

dDepartment of Chemistry, University of Zurich, Winterthurerstrasse 190, 8057 Zurich, Switzerland

eUnidad de Polímeros y Electrónica Orgánica, Instituto de Ciencias, Benemérita Universidad Autónoma de Puebla, Val3-Ecocampus Valsequillo, Independencia O2 Sur 50, San Pedro Zacachimalpa, Puebla 72960, CP, México

fDepartment of Medicinal Chemistry, Faculty of Pharmacy, Mansoura University, Mansoura 35516, Egypt. E-mail: elemam@mans.edu.eg

† Electronic supplementary information (ESI) available. CCDC 2302018 and 2302019. For ESI and crystallographic data in CIF or other electronic format see DOI: https://doi.org/10.1039/d3ra07169c

1. Introduction

1,3,4-Oxadiazoles are an imperative class of heterocyclic compounds with diverse pharmacological properties.[1] 1,3,4-Oxadiazole is a valuable structural core in currently employed chemotherapeutic agents such as the broad spectrum antibacterial drug furamizole,[2] the anticancer agent zibotentan,[3] the herbicidal and fungicidal agent oxadiazon[4] and the antiretroviral drug raltegravir.[5] The chemotherapeutic efficacy of anticancer 1,3,4-oxadiazoles is attributed to targeting thymidylate synthase,[6] epidermal growth factor receptors (EGFR),[7] vascular endothelial growth factor receptors (VEGF),[8] histone deacetylases (HDAC),[9] tubulin polymerase,[10] methionine aminopeptidase (MetAP),[11] focal-adhesion kinase (FAK),[12] telomerase,[13] and nuclear factor κB.[14] It has been reported that several solid tumors overexpress thymidine phosphorylase, which plays a crucial role in angiogenesis.[15] In addition, the antifungal activity of several 1,3,4-oxadiazole derivatives is

attributed to potent succinate dehydrogenase inhibitory activity.[16] Furthermore, in the last two decades, organo-fluorine compounds represent one of the most fast-growing classes of bioactive compounds.[17]

In view of the previously reported observations and as a continuation of an interest in developing chemotherapeutic agents,[18] and structural characterization of 1,3,4-oxadiazole-based derivatives,[19] we report herein the synthesis, characterization, supramolecular features, nature of intermolecular interactions, preliminary antimicrobial and anti-proliferative activities of two 3-fluorophenylaminomethyl-1,3,4-oxadiazole-2(3H)-thione derivatives. The antioxidant activity of the N-Mannich base of 1,3,4-oxadiazole derivatives bearing 1,4,-benzodioxan was reported.[20] Similarly, the crystal structures of the adamantyl group attached to the central 1,3,4-oxadiazole moiety were reported and these compounds were similar to those of the title compounds.[21] Non-covalent interactions (NCI), particularly hydrogen bonds, have become one of the most important topics not only in synthetic chemistry, but also in biological and material systems.[22] The occurrence and importance of C–H groups as donors in hydrogen bond formation in biological macromolecules such as proteins and nucleic acids were described.[23] In contrast, σ-holes, another type of NCI, possess electron-deficient regions that arise when electron density is anisotropically distributed on group 14 elements (tetrels), 15 elements (pnictogens), 16 elements (chalcogens) and 17 elements (halogens) elements when they are covalently bonded to electron-withdrawing groups.[24] The title compounds exhibit some unique intermolecular interactions such as halogen bond (Cl···Cl and Cl···π), and C–F···F–C and F···O noncovalent interactions compared to the closely related reported structures.

In this work, we present structural analysis of two closely related 1,3,4-oxadiazole-2-thione N-Mannich base derivatives to investigate the intermolecular interactions formed in these solid-state structures, the energetics, nature of the intermolecular interactions and *in vitro* bioactivities. Furthermore, a molecular docking analysis was performed to delineate the favorable orientation of these compounds at the active sites of four different drug targets. The title compounds exhibit a variety of conventional and non-conventional intermolecular contacts. The PIXEL energy calculation, Hirshfeld surface analysis, a DFT study, QTAIM, molecular electrostatic potential, and NCI plot analysis were carried out to characterize the intermolecular interactions observed in these compounds. Some of these computational tools have been successfully applied to various solid-state structures and modeled complexes to analyze various non-covalent interactions with respect to their geometrical preferences, strength and nature.[25]

2. Materials and methods

2.1. Synthesis and crystallization

To a solution of 5-(4-chlorophenyl)-1,3,4-oxadiazole-2(3H)-thione **C** (1.06 g, 5.0 mmol) in ethanol (10 mL), 37% formaldehyde solution (1.0 mL) and 2-trifluoromethylaniline (0.81 g, 5.0 mmol) or 2,5-difluoroaniline (0.65 g, 5.0 mmol) were added and

the reaction mixture was stirred at room temperature for 5 hours and allowed to stand overnight. The precipitated crude products were filtered, washed with water, dried and crystallized from aqueous ethanol to yield the target compounds **1** and **2**. Suitable single crystals for X-ray diffraction were obtained by slow evaporation of a solution of the title compound in ethanol : chloroform (1 : 1, v/v) at room temperature.

5-(4-Chlorophenyl)-3-[(2-trifluoromethylphenylamino) methyl]-1,3,4-oxadiazole-2(3H)-thione (1). Colourless needle crystal. Melting point: 183–185 °C (uncorrected). Yield: 1.64 g (85%). Analysis calcd for $C_{16}H_{11}ClF_3N_3OS$: C, 49.81; H, 2.87; N, 10.89; S, 8.31%. Found: C, 49.80; H, 2.88; N, 10.82; S, 8.28%. ^1H NMR (CDCl₃, 500.16 MHz): δ 5.58 (s, 2H, CH₂), 5.71 (s, 1H, NH), 6.89 (d, 1H, Ar–H, J = 8.0 Hz), 7.26 (t, 1H, Ar–H, J = 8.0 Hz), 7.83 (d, 2H, Ar–H, J = 7.5 Hz). ^{13}C NMR (CDCl₃, 127.77 MHz): δ 57.69 (CH₂), 113.66, 119.03, 120.65, 123.55, 126.93, 127.74, 128.44, 129.59, 133.35, 138.89, 141.91 (Ar–H & CF₃), 158.72 (oxadiazole C⁵), 176.48 (C=S).

5-(4-Chlorophenyl)-3-[(2,5-difluorophenylamino)methyl]-1,3,4-oxadiazole-2(3H)-thione (2). Colourless needle crystal. Melting point: 164–166 °C (uncorrected). Yield: 1.27 g (72%). Analysis Calcd. for $C_{15}H_{10}ClF_2N_3OS$: C, 50.93; H, 2.85; N, 11.88; S, 9.06%. Found: C, 50.88; H, 2.87; N, 11.78; S, 9.02%. ^1H NMR (CDCl₃, 500.16 MHz): δ 5.53 (s, 2H, CH₂), 6.44 (t, 1H, NH, J = 9.0 Hz), 6.88–7.18 (m, 3H, Ar–H), 7.47–7.52 (m, 2H, Ar–H), 7.84 (d, 2H, Ar–H, J = 7.5 Hz). ^{13}C NMR (CDCl₃, 127.77 MHz): δ 57.56 (CH₂), 101.46, 105.15, 115.53, 120.59, 127.77, 129.63, 133.70, 138.96, 146.78, 160.32 (Ar–H), 158.67 (Oxadiazole C⁵), 176.52 (C=S).

2.2. Single crystal X-ray analysis

For crystals **1** and **2**, the X-ray intensity data were collected at 160 K on a Rigaku OD SuperNova/Atlas area-detector diffractometer using Cu Kα radiation (λ = 1.54184 Å) from a microfocus X-ray source and an Oxford Instruments Cryojet XL cooler. The suitable single crystal was mounted using polybutene oil on a flexible loop fixed on a goniometer head and immediately transferred to the diffractometer. Pre-experiment, data collection, data reduction and analytical absorption correction[26] were performed with the program CrysAlisPro (CrysAlis, Version 1.171.40.16c, Rigaku Oxford Diffraction, 2018). Using *Olex2*,[27] the structure was solved with the SHELXT[28] small molecule structure solution program and refined with the *SHELXL2018/3* program package[29] by full-matrix least-squares minimization on F^2. The position of amine H atom was located from a difference Fourier map and refined freely along with its isotropic displacement parameters. All the remaining H atoms were placed in calculated positions (C–H = 0.95–0.99 Å) and constrained to ride on their parent atoms, with the $U_{iso}(H) = 1.2U_{eq}(C)$. PLATON was used to check the result of the X-ray analysis.[30] Mercury program was used to generate crystal packing and molecular dimers.[31]

2.3. Computational methods

The crystal structure geometry with the normalized H positions according to the typical neutron diffraction values (C–H = 1.083

and N–H = 1.009 Å) was used for all calculation. The nature of intermolecular interactions and their contributions were studied using the Hirshfeld surface[32] and 2D-fingerprint plots[33] with the CrystalExplorer 17.5 program.[34] The calculations reported herein were performed using the Turbomole 7.0 program.[35] The crystallographic coordinates were used for the calculations of the supramolecular assemblies. We have used the crystallographic coordinates for the assemblies because we are interested in evaluating the interactions as they stand in the solid state since the purpose of this manuscript is not finding the most favourable orientation of the molecules in the isolated dimers in the gas phase. The level of theory used for the calculations was RI-BP86-D3/def2-TZVP.[36] The molecular electrostatic potential (MEP) surface plots were generated using the wavefunctions obtained at the same level of theory and the 0.001 a.u. isosurface to simulate the van der Waals envelope. The topological analysis of the electron density was carried out according to the QTAIM and noncovalent interaction plot index (NCIplot) methods proposed by Bader[37] and W. Yang et $al.$,[38] respectively. Both were represented using the VMD program[39] using the following settings for the NCI plot index representation: $s = 0.5$ a.u.; cut-off $\rho = 0.04$ a.u. and colour scale $-0.03 \leq sign(\lambda_2) \rho \leq 0.03$ a.u. The electron localization function (ELF)[40] analysis was performed using the MultiWFN program[41] at the PB86-D3/def2-TZVP level of theory.

2.4. In $vitro$ antimicrobial activity

The in $vitro$ antimicrobial activity of the 1,3,4-oxadiazole derivatives 1 and 2 towards a panel of standard pathogenic bacterial and fungal strains namely; $Staphylococcus$ $aureus$ ATCC 6571, $Bacillus$ $subtilis$ ATCC 5256, $Micrococcus$ $luteus$ ATCC 27141 (Gram-positive bacteria), $Escherichia$ $coli$ ATCC 8726, $Pseudomonas$ $aeruginosa$ ATCC 27853 (Gram-negative bacteria), and the yeast-like pathogenic fungus $Candida$ $albicans$ MTCC 227 was evaluated. The preliminary screening was carried out following the semi-quantitative agar-disc diffusion method with Müller-Hinton agar medium.[42] The minimal inhibitory concentration (MIC) of compounds 1 and 2 was assessed against the same microorganism used in the preliminary screening using the micro-dilution susceptibility method in Müller-Hinton Broth.[43]

2.5. In $vitro$ anti-proliferative activity

The in $vitro$ anti-proliferative activity of compounds 1 and 2 was evaluated against HepG-2 (hepatocellular carcinoma), PC-3 (human prostate cancer), HCT-116 (colorectal carcinoma) and MCF-7 (mammary gland breast cancer) tumor cell lines using the 3-[4,5-dimethylthiazoyl-2-yl]-2,5-diphenyltetrazolium bromide (MTT) colorimetric assay.[44]

2.6. Molecular docking simulations

Molecular docking analysis was carried out for compounds 1 and 2 and co-crystallized ligands in the respective protein-inhibitor complexes using the Schrödinger suite (Schrödinger suite, LLC, New York, NY, 2021). In this study, we used two cancer targets namely, human thymidine phosphorylase (PDB ID: 1UOU; co-crystallized ligand ID: CMU),[45] human

thymidylate synthase (PDB ID: 6QXG; co-crystallized ligand ID: UFP)[46] and a bacterial target namely, thymidine phosphorylase from $Escherichia$ $coli$ K12 strain (PDB ID: 4EAD; co-crystallized ligand ID: 0NP) and pyrimidine-nucleoside phosphorylase from $Staphylococcus$ $aureus$ strain COL (PDB ID: 3H5Q; co-crystallized ligand ID: THM). In all four cases, one subunit (chain A) was retrieved from the protein data bank (www.rcsb.org). The co-crystallized ligands in these targets and the compounds 1 and 2 were prepared using the ligprep module and the target proteins were prepared using the protein preparation wizard. For both ligands and proteins, OPLS4 force field was applied.[47] The glide XP docking score was used to predict the most favourable orientation of the ligand at the protein active site.[48] The protein-ligand interactions for the best predicted poses were analyzed using the PLIP Web server.[49]

3. Results and discussion

3.1. Chemical synthesis

4-Chlorobenzohydrazide B was prepared from the commercially-available methyl 4-chlorobenzoate A via treatment with hydrazine in ethanol.[50] 1,3,4-Oxadiazole-2(3H)-thione C was obtained via reaction of the carbohydrazide B with carbon disulfide in ethanolic potassium hydroxide as previously described.[6] 1,3,4-Oxadiazole-2(3H)-thiones were reported to undergo aminomethylation through reaction with primary aromatic amines and formaldehyde to yield the corresponding N-Mannich bases.[18] Consequently, treatment of C with 2-trifluoromethylaniline or 2,5-difluoroaniline and formaldehyde solution and various primary aromatic amines in ethanol at room temperature yielded the target 3-arylaminomethyl N-Mannich bases 1 and 2 in good yields (Scheme 1). The
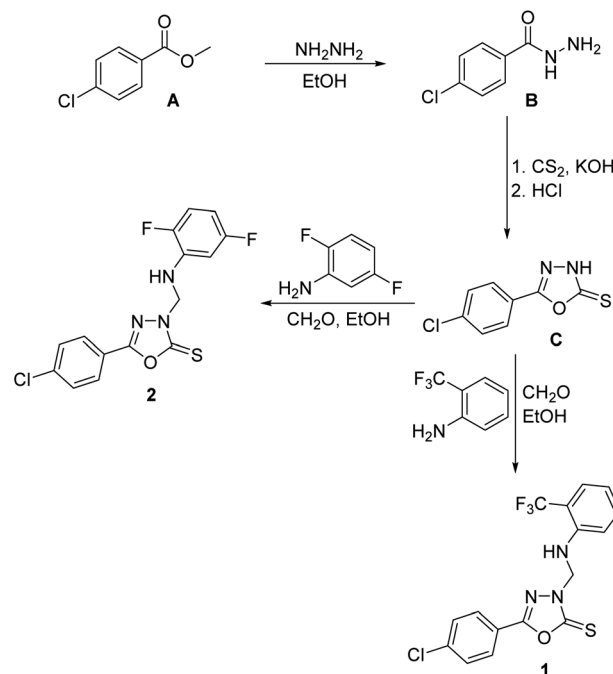
Scheme 1 The synthetic pathway for compounds 1 and 2.

structures of compounds **1** and **2** were confirmed by elemental analyses, ^{1}H NMR and ^{13}C NMR spectral data in addition to single crystal X-ray analysis.

3.2. Molecular and crystal structures

In order to gain insights into how the substituents affect molecular conformation, crystal packing, and intermolecular interactions, the single crystal X-ray analyses of compounds **1** and **2** were determined at 160 K. The X-ray analysis revealed that both compounds crystallize in the orthorhombic crystal system with the non-centrosymmetric space groups $P2_12_12_1$ (compound **1**) and $Iba2$ (compound **2**). A summary of X-ray crystallographic data and refinement parameters is presented in Table 1. As shown in Fig. 1, both compounds contain a 4-chlorophenyl ring (ring A) attached to an oxadiazole ring (ring B). There is a difference between these two compounds in their substituted ring C. In compound **1**, the trifluoromethyl group is present at the *ortho* position. In compound **2**, the fluorine substitutions occur at the *ortho* and *meta* positions. The amino methylene group bridges the rings B and C in both compounds.

Molecular geometry from the CSD database is used as knowledge base in an algorithm to verify molecular geometry using the mogul geometry check utility.[51] We performed the mogul geometry check for compounds **1** and **2** and the results showed unusual bond length and valence angles involving the oxadiazole ring for **1**. The length of the oxadiazole ring's C8–N2 bond (1.349 Å) is slightly higher than the mean value of 1.337 Å,
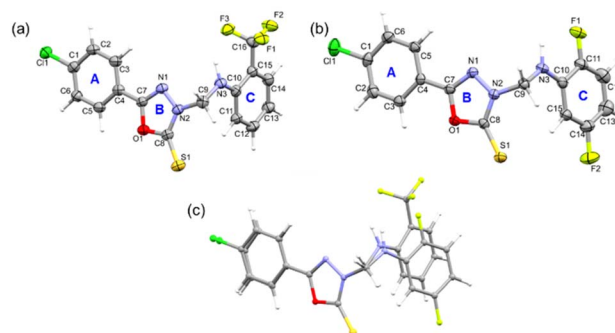

Fig. 1 The ORTEP representations of compounds (a) **1** and (b) **2** are drawn at the 50% probability level, and (c) a structural overlay illustrates the deviation around ring C between compounds **1** and **2**.

and the four valence angles of the oxadiazole ring also deviate from the respective mean value. In addition to the valence angles of the oxadiazole, one of the valence angles (C11–C10–C15 = 117.44°; mean value = 119.87°) of ring C is also affected. It is to be noted that no such deviated geometrical parameters are observed for structure **2**. The deviation of geometrical parameters could indicate the effect due to the trifluoromethyl group in ring C of **1**.

Furthermore, in both structures, rings A and B are nearly coplanar (5.88° in **1** and 5.64° in **2**) and the dihedral angle between mean planes of A/B and C rings is 84.64° in **1** and

Table 1 Crystal data and structure refinement for compounds **1** and **2**

	Compound **1**	Compound **2**
Empirical formula	$C_{16}H_{11}ClF_3N_3OS$	$C_{15}H_{10}ClF_2N_3OS$
Formula weight	385.79	353.77
Temperature (K)	160 (1)	160 (1)
Crystal system	Orthorhombic	Orthorhombic
Space group	$P2_12_12_1$	$Iba2$
a (Å)	4.7906 (2)	28.8781 (9)
b (Å)	13.1169 (6)	13.8936 (4)
c (Å)	25.4767 (12)	7.7325 (3)
α (°)	90	90
β (°)	90	90
γ (°)	90	90
Volume (Å^3)	1600.90 (12)	3102.43 (17)
Z	4	8
ρ_{calc} (g cm^{-3})	1.601	1.515
μ (mm^{-1})	3.741	3.709
$F(000)$	784.0	1440.0
Crystal size (mm^3)	0.27 × 0.03 × 0.02	0.11 × 0.05 × 0.02
Radiation	Cu Kα (λ = 1.54184)	Cu Kα (λ = 1.54184)
2θ range for data collection/°	6.94 to 148.798	6.122 to 148.86
Index ranges	$-5 \leq h \leq 5, -14 \leq k \leq 16, -31 \leq l \leq 31$	$-36 \leq h \leq 36, -13 \leq k \leq 17, -9 \leq l \leq 9$
Reflections collected	15 968	15 474
Independent reflections	3244 [R_{int} = 0.0711, R_{sigma} = 0.0460]	3163 [R_{int} = 0.0466, R_{sigma} = 0.0326]
Data/restraints/parameters	3244/0/230	3163/1/212
Goodness-of-fit on F^2	1.035	1.061
Final R indexes [$I > = 2\sigma$ (I)]	R_1 = 0.0399, wR_2 = 0.0994	R_1 = 0.0270, wR_2 = 0.0581
Final R indexes [all data]	R_1 = 0.0473, wR_2 = 0.1042	R_1 = 0.0334, wR_2 = 0.0607
Largest diff. peak/hole (e Å^{-3})	0.38/−0.32	0.18/−0.16
Flack parameter	0.013(17)	−0.004(10)
CCDC no.	2302018	2302019

71.46° in **2**. We also note that both molecules adopt a L-shaped molecular conformation which is very similar to that of the structures, namely 2-(4-fluorobenzylthio)-5-(5-bromothiophen-2-yl)-1,3,4-oxadiazole and 4-(4-chlorophenyl)-3-[(4-fluorobenzyl)sulfanyl]-5-(thiophen-2-yl)-4*H*-1,2,4-triazole reported earlier.[19,52] One of the arms of L comprises rings A and B, while the other arm of L consists of ring C. Fig. 1c shows the structural deviation around ring C, whereas rings A and B are overlaid very well. This structural deviation could be due to the substituted ring C mentioned above.

In the solid state, both compounds exhibit different types of weak hydrogen bonds and other unorthodox contacts because of the presence of suitable donors, acceptor groups, and aromatic rings. However, we are particularly interested in the ability of the chlorophenyl ring to establish halogen bonding interactions as a σ-hole donor. It is well known that chlorine is a very weak σ-hole donor and its ability to form halogen bonds has been an issue of discussion in the literature.[53] Several nonclassical noncovalent interactions observed in molecular solids were described in the literature to highlight their cooperativity with conventional noncovalent interactions and the role of individual interaction in supramolecular assemblies.[54]

3.3. Qualitative analysis of intermolecular interactions: Hirshfeld surface and 2D-fingerprint plots

With a fingerprint plot, HS analysis has become an invaluable tool for exploring the nature of intermolecular interactions within crystal structures. In this way, characteristic interactions within structures and surfaces around molecules can be easily identified. In a d_{norm} surface, intermolecular contacts can be easily compared in terms of van der Waals radii *via* a simple red-white-blue colour scheme.

In compound **1**, the intense red regions represent close inter-contacts such as $C(\pi)\cdots C(\pi)$, C–F⋯F–C, and three-centered intermolecular C–H⋯F interactions (Fig. 2a). These short contacts have a significant impact on crystal packing. In compound **2**, six different intermolecular interactions such as

N–H⋯S, C–H⋯F, $C(\pi)\cdots C(\pi)$, S(lp)⋯$C(\pi)$, F⋯O contacts and a σ-hole of type C–Cl⋯$C(\pi)$ halogen bond with varying degrees of red spots on the HS (Fig. 2b). It is thought that these contacts are essential for the stabilization of crystal structure **2**.

The 2D fingerprint plots obtained from the Hirshfeld surface calculation show how various intermolecular interactions contribute to crystal packing and how substituents affect the contribution of these interactions. The selected 2D fingerprint plots for compounds **1** and **2** are shown in Fig. S1 (ESI†). The main contributions come from H⋯H contacts, which range from 20.6 to 21% and whose contributions to the crystal packing of **1** and **2** are very similar. The intermolecular H⋯F contacts significantly contribute to the crystal packing of both compounds. Since structure **2** has only two F atoms, the contribution of this contact is expected to be less compared to structure **1**. Moreover, the fingerprint plots show that this contact is distributed differently between the two structures. For example, double sharp tips have a tip distance ($d_e + d_i$) of ∼2.3 Å in **2**, while blunt tips have a slightly longer tip distance of 2.5 Å in **1**. We also note a slight difference (2.8%) in the contribution of H⋯C contacts between the two structures. The observed close contact appears around 2.80 Å and can form intermolecular C–H⋯$C(\pi)$ interactions in **1**, while the corresponding contact in **2** appears to be longer than 3.0 Å, suggesting that this contact is not essential for stabilization.

Another significant contribution comes from the H⋯Cl interactions, and the tip distance is about 2.9 Å in the fingerprint plots in both structures and has a slightly higher contribution to the total HS area in **2** compared to **1**. Although the relative contribution of H⋯S contact differs between these two structures (10.1% in **1** and 7.0% in **2**), the fingerprint plots also show differences in the d_{norm} spacing. The intermolecular H⋯S contacts appear at 2.5 Å in **2**, while the corresponding short contact distance is 3.0 Å in **1**. The distribution of H⋯S contact confirms the presence of the N–H⋯S interaction, and the same type of intermolecular interaction is not possible in **1**. It is, however, possible to establish a C–H⋯S interaction. It is interesting to note that the intermolecular F⋯F contact in **1** is established with a tip distance of 2.8 Å and contributes about 4.0% to crystal packing. However, in **2**, this contact disappears. The relative contribution of the H⋯N contact is almost the same in both structures. However, this contact is relatively shorter in **2** (∼2.7 Å) than in structure **1** (over 2.8 Å). This feature indicates that structure **2** tends to establish a C–H⋯N interaction, whereas this contact is weak in structure **1** due to the longer separation between the H and N atoms. Similarly, the C⋯C contact, representing the π-stacking interaction, contributes 4.7% to the crystal packing of **1**, while the corresponding contact contributes only about 1.7% in **2**. Red-blue triangles on the surfaces of rings A and B in the shape index diagram and green dots at 3.6 Å in the 2D-FP plots indicate that these two rings can stack on each other (Fig. S2, S3, ESI†).

The halogen bonds show an interesting feature in the 2D fingerprint plots. In **1**, a homo-halogen bond of the type Cl⋯Cl interaction contributes about 1.7% to the crystal packing and is located as short as 3.5 Å, indicating its short nature and found important for stabilization. The corresponding contact is in **2**
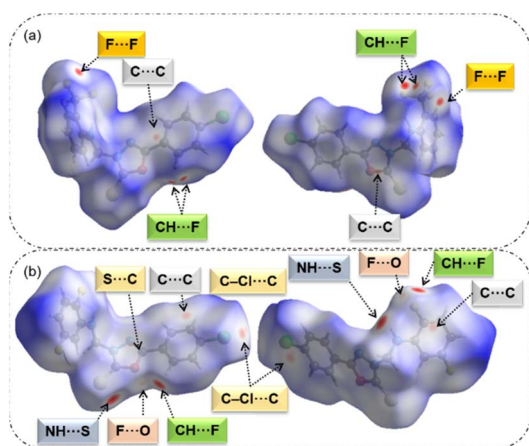

Fig. 2 Red spots on the Hirshfeld surfaces with two different orientations show the close inter-contacts observed in structures (a) **1** and (b) **2**.

beyond 3.9 Å, indicating its weak nature. The relative contribution of another potential halogen bond of the type Cl···C(π) is almost the same in both structures. However, this contact is relatively shorter in **2** (∼3.4 Å) than in structure **1** (3.6 Å). This observation suggests that the Cl···Cl halogen bond in **1** and the Cl···C(π) halogen bond in **2** play an important role in stabilizing the respective crystal structure. We also note that the F atom establishes a noncovalent interaction with the oxadiazole O atom. The 2D-FP plots show that the F···O interaction in **2** is relatively shorter than in structure **1** although its contribution to crystal packing is comparable between the two structures. Furthermore, there is a short S···C contact at 3.5 Å with a contribution of 3.8% in structure **2** and the corresponding contact at slightly over 3.5 Å with a contribution of 1.1% in **1**. The 2D-FP plots for the other possible inter-contacts are relatively longer than the sum of the vdW radii of the interacting atoms in these structures.

3.4. Supramolecular self-assembly in 1

In the solid state, molecule **1** is packed columnar along the crystallographic *bc* and *ac* planes, as shown in Fig. 3a and b. The energetically significant dimers in this structure were identified by CLP-PIXEL calculations (Fig. 3c–f). The results showed that five important dimers contribute to stabilizing the crystal structure. Various types of intermolecular interactions are formed in these dimers, including C–H···F, C–H···Cl, C–H···S, C–H···π, π-stacking, F···O, C–F···F–C contacts, and a homo halogen bonding type of C–Cl···Cl interaction. The intermolecular interaction energies for these dimers were calculated using the CLP-PIXEL method and ranged from −13.3 to −1.3 kcal mol^{-1}. Accurate dimerization energies were calculated using the DFT method at the B97-D3/def2-TZVP level of theory to compare these energies with those calculated using the CLP-PIXEL method. As shown in Table 2, the dimerization energies calculated with both methods are comparable except

for dimer D1. The CLP-PIXEL method underestimates the energy of the D1 dimer, which could be due to the dispersion effect of the observed intermolecular interactions in D1.

A highly stable dimer D1 consists of two adjacent L-shaped molecules held together by intermolecular π-stacking, C–H··· π and C–F···F–C interactions (Fig. 3c). The π-stacking interaction is formed between rings A and B (centroid-to-centroid distance = 3.484 (2) Å), while the bridging methylene group participates in an intermolecular C–H···π interaction with the π-system of ring C. The C–F···F–C interaction is formed between adjacent CF$_3$ groups. The components of electrostatic and dispersion energies contribute 26 and 74%, respectively, to stabilizing D1. The higher contribution of dispersion energies could be due to the effect of the π-stacking and C–H···π and C–F···F–C interactions.

Four different types of halogen–halogen bonding (involving Cl, Br and I) geometries were described in the literature as shown in Scheme 2.[55] The homo fluorine (F···F) interactions are also shown as one of the four types of geometries. To gain more insight into the geometrical preference of C–F···F–C contacts from trifluoromethyl moiety, we searched the Cambridge Structural Database (CSD, version 2022.3.0) using a template containing trifluoromethylphenyl residues rather than Ph-F residues, and the search yielded 584 hits with 970 C–F···F–C contacts. The separation of F···F contacts ranges from 2.503 to 2.940 Å, and the shortest one was observed for the entry with refcode HEWFAQ (d = 2.503 Å), and the longest separation was observed for the entry with refcode DIDQAK (d = 2.940 Å). More than 80% of contacts fall between 2.803 and 2.940 Å (Fig. S4, ESI†). In this study, we observed the F···F distance is 2.832 (4) Å, which lies in the most preferred region. Tothadi *et al.* described the classification of homo-halogen bonding based on the difference in angles ($0° \leq |\theta_1 - \theta_2| \leq 15°$: type I; $30° \leq |\theta_1 - \theta_2|$: type II and $15° \leq |\theta_1 - \theta_2| \leq 30°$: quasi type I/II).[56] According to this classification, 52.4% of the contacts exhibit type I geometry, similar to Cl···Cl contacts surveyed earlier. 16.1% of the contacts belong to quasi-type I/II geometry (Fig. S5, ESI†). In the present study, F···F contact belongs to type I/II geometry with the $|\theta_1 - \theta_2| = 29.85°$. The remaining contacts belong to type II geometry. The CSD search also indicates that some F···F contacts adopt a Z-shaped geometry. Furthermore, we calculated the deformation density for the dimer, showing the C–F··· F–C interaction (Fig. 3g).

The neighbouring molecules stacked along the crystallographic *b* axis in a column are connected by a large number of intermolecular interactions, including intermolecular C–H···F/ S/C(π) interactions and unconventional F···O contacts. These interactions lead to the formation of the dimer D2, and the contribution of the electrostatic and dispersion energies to the stabilization is 36% and 64%, respectively. There are rectangular molecular arrangements in the repetitive structural motif of **1** (dimer D3) (see Fig. 3, dashed rectangular box). This motif is stabilized by an intermolecular C–H···Cl interaction and links the molecules into a supramolecular *C*(14) chain that runs parallel to the crystallographic *b* axis. Notably, the dispersion energy contributes more (75%) towards stabilizing dimer D3. A weak molecular dimer (D5) is stabilized by a directional σ-hole
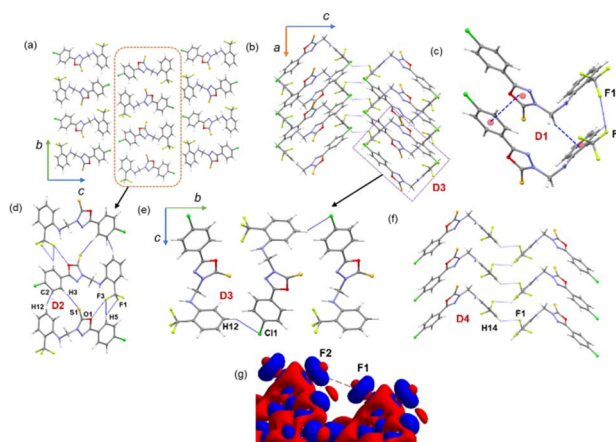

Fig. 3 Crystal packing of **1** projected onto the crystallographic (a) *bc* plane, (b) *ac* plane, and (c–f) dimers observed in **1**, supramolecular self-assembly mediated by various intermolecular contacts, and (g) deformation density showing charge depletion (red) and charge concentrated region (blue) around interacting fluorine atoms.

Table 2 Intermolecular interaction energies (in kcal mol^{-1}) for different dimers were obtained from the crystal structure of **1** using the CLP-PIXEL and DFT methods. The BSSE corrected dimerization energies calculated by the DFT method were given for comparison

Dimer	CD	Symmetry	Important interactions	Geometry H···A (Å), ∠D–H···A (°)	PIXEL/MP2/6-31G**					B97D3/def2-tzvp
					E_{coul}	E_{pol}	E_{disp}	E_{rep}	E_{tot}	ΔE_{cp}
D1	4.791	$x-1, y, z$	Cg1···Cg2	3.484 (2)	−4.8	−2.5	−20.6	14.6	−13.3	−17.7
			C9–H9B···Cg3	2.80, 139						
			C16–F1···F2–C16	2.832 (4), 149.2 (2)						
D2	6.647	$-x+1, y-1/2, -z+3/2$	C5–H5···F1	2.44, 134	−2.9	−1.8	−8.2	6.1	−6.8	−5.7
			C5–H5···F3	2.43, 169						
			C3–H3···S1	2.98, 126						
			C12–H12···C2(π)	2.82, 134						
			C16–F3···O1	3.049 (4), 151.7 (2)						
D3	7.965	$-x, y-1/2, -z+3/2$	C12–H12···Cl1	2.91, 136	−1.6	−0.7	−4.4	2.5	−4.3	−4.0
D4	12.479	$x-1/2, -y+1/2, -z+2$	C14–H14···F1	2.60, 136	−0.5	−0.1	−1.8	0.7	−1.7	−1.4
D5	14.397	$x+1/2, -y+1/2, -z+1$	C1–Cl1···Cl1	3.523 (1), 162.5 (1)	−0.6	−0.3	−2.2	1.7	−1.3	−1.2
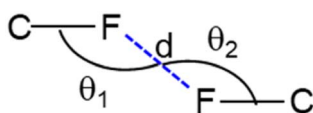
Scheme 2 Geometrical parameters of C–F···F–C interactions involving trifluoromethyl moieties found in CSD database. Different types geometries are defined as: type I (90° < $\theta_1 \approx \theta_2$ < 180°; parallel displaced geometry), type II ($\theta_1 \sim$ 90°; $\theta_2 \sim$ 180°; L-shaped geometry) and type III ($\theta_1 \approx \theta_2$ = 180°; linear geometry) and type IV ($\theta_1 \approx \theta_2$ = 90°; Z-shaped geometry).

bonding namely C–Cl···Cl halogen bonding interaction. This dimer is also predominantly driven by the dispersion energy component, contributing 71% towards the total stabilization energy. This halogen bond exhibits an L-shaped geometry (type II geometry with $|\theta_1 - \theta_2|$ = 70.37°). To investigate the existence of σ-hole contact in **1**, we carried out molecular electrostatic potential surface analysis, and the results are presented in a separate section.

3.5. Supramolecular self-assembly in 2

In the crystalline state, molecule **2** is arranged in columnar along the crystallographic *ab* plane, as shown in Fig. 4a. From the CLP-PIXEL calculation, one can extract the energetically significant dimers in this crystal structure (Table 3). There are five such dimers (D1–D5) stabilized by varieties of intermolecular interactions such as N–H···S, C–H···NF/Cl, C(π)···C(π) contact, S(lp)···π contact (Fig. 4a–e). Furthermore, a directional halogen bond of type C–Cl···C(π) and a fluorine bond of type C–F···O interaction (Fig. 4b). It is important to emphasize that some of the intermolecular interactions such as N–H···S, C–H···N, lp···π, C–Cl···C(π) and C–F···O contacts are specific to compound **2**. These specific interactions play a major role in stabilizing the solid-state structure. Furthermore, the intermolecular interaction energies for these dimers are calculated using the CLP-PIXEL method, ranging from −12.5 to −1.7 kcal mol^{-1}. The dimerization energies calculated by the DFT and CLP-PIXEL methods are comparable (Table 3). Slight

deviations in energies in some dimers occur due to the effect of dispersive forces and the types of interactions present in them.

In this structure, the strongest dimer (D1) stabilizes with the intermolecular lp···π interaction involving S1 and the π-system of ring B (Fig. 4c). This interaction links the molecules into a chain parallel to the crystallographic *c* axis. It is also noted that electrostatic energy contributes 40% towards the total stabilization energy for this dimer. In the solid state, dimer D2 extends along the *b* axis to generate a molecular ribbon, and adjacent ribbons formed by dimer D2 are interconnected by dimer D5 (Fig. 4b). These two dimers collectively generate a supramolecular chain along the *ab* plane. The former dimer D2 stabilizes with five intermolecular interactions. The N–H···S interaction is formed between the amine group and the S atom of the oxadiazole moiety. Both fluorine atoms (F1 and F2) of ring C have been involved in intermolecular C–H···F interactions. One of the fluorine atoms (F1) is engaged in an unorthodox fluorine bond of type F···O contact. The 3D deformation density
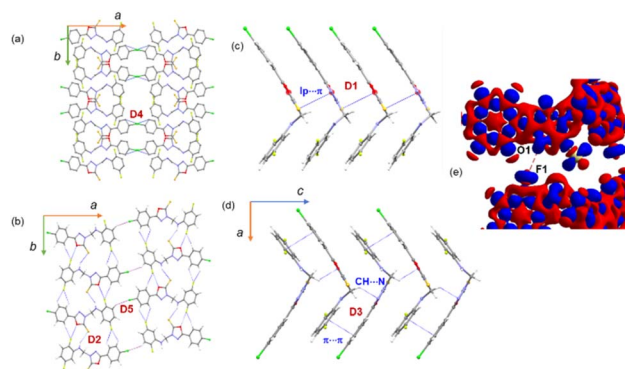
Fig. 4 (a) Adjacent columns are interlinked by directional C–Cl···C(π) halogen bond, (b) supramolecular ribbon formed by motif D2 and adjacent supramolecular ribbons are interlinked by weak C–H···Cl hydrogen bonds, (c) L-shaped molecular layer held together by S(lp)···π interaction, and (d) molecular dimer D3 is formed by intermolecular C–H···N interaction and supported by a weak C(π)···C(π) interaction, (d) 3D deformation electron density shows intermolecular F···O contact (red: charge depletion region and blue: charge concentrated region).

Table 3 Intermolecular interaction energies (in kcal mol^{-1}) for different dimers were obtained from the crystal structure of **2** using the CLP-PIXEL and DFT methods. The BSSE corrected dimerization energies calculated by the DFT method were given for comparison
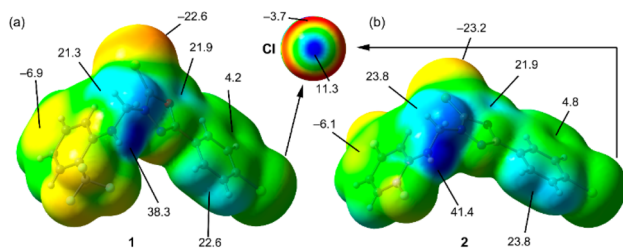
Dimer CD	Symmetry	Important interactions	Geometry H···A (Å), ∠D–H···A (°)	PIXEL/MP2/6-31G**					B97D3/def2-tzvp
				E_{coul}	E_{pol}	E_{disp}	E_{rep}	E_{tot}	ΔE_{cp}
D1	5.089 $x, -y + 1, z - 1/2$	S1···Cg1	3.343 (1)	−6.2	−3.2	−14.2	11.0	−12.5	−14.7
D2	7.089 $-x + 3/2, y - 1/2, z$	N3–H3A···S1	2.50, 149	−8.4	−4.4	−7.2	9.8	−10.2	−8.3
		C5–H5···F2	2.56, 122						
		C6–H6···F2	2.62, 119						
		C3–H3···F1	2.23, 173						
		C11–F1···O1	2.923 (1), 160.36(1)						
D3	5.493 $-x + 3/2, -y + 3/2, z - 1/2$	C9–H9A···N1	2.73, 137	−3.1	−1.4	−12.6	7.6	−9.4	−12.1
		C11···C6	3.303 (4)						
D4	13.587 $-x + 1, y, z - 1/2$	C1–Cl1···C6(π)	3.390(3), 170.9(1)	−0.9	−0.5	−3.8	3.2	−2.1	−2.4
D5	14.890 $x - 1/2, -y + 3/2, z$	C12–H12···Cl1	2.90, 153	−0.7	−0.3	−1.6	1.0	−1.7	−1.5

calculated from theoretical charge density analysis for the F···O contact shows the small polarizability of electron density around the fluorine atom (Fig. 4e). The charge depletion region of fluorine (red) pointed towards the charge concentrated region on the O1 atom (blue). The CSD search reveals a very small number of F···O contacts exist. The CLP-PIXEL calculation reveals that the contribution of electrostatic and dispersion energies is 64 and 36% towards the stabilization of dimer D2, whereas the dispersion energy contributes (62%) more to the stabilization of dimer D5 than the electrostatic energy.

As illustrated in Fig. 4d, a supramolecular chain is generated by the dimer D3 which stabilizes with two intermolecular interactions. In this dimer, the bridge methylene group acts as a donor and one of the N atoms of the oxadiazole ring is involved as an acceptor for the intermolecular C–H···N interaction. The stability of D3 is supported by a C(π)···C(π) contact (3.303 (4) Å) between rings A and C in an offset mode and the dispersion energy contributes 74% towards stabilization. Dimer D4 stabilizes with a weak C1–Cl1···C6(π) halogen bond. As shown in Fig. 4a, this halogen bond interlinks the adjacent molecular sheets formed on the crystallographic *ab* plane.

3.6. Nature of halogen bonding interactions in 1 and 2

Initially, we used molecular electrostatic potential surface calculations to investigate the existence of σ-hole at the Cl atom

in compounds **1** and **2**. The surfaces are represented in Fig. 5, showing that in both compounds, the MEP maximum is located at the NH bond (+38.3 and +41.4 kcal mol^{-1} for **1** and **2**, respectively), and the MEP minimum is located at the S-atom of the thione group (−22.6 and −23.2 kcal mol^{-1}, respectively). The MEP is also large and positive over the five-membered ring (+21.9 kcal mol^{-1} in both compounds) disclosing that the five-membered ring is electron deficient and exerts a significant electron withdrawing effect on the chlorophenyl ring. This increases the MEP value at the chlorine's sigma-hole and reduces the nucleophilicity of the negative belt (MEP value is more positive). In Fig. 5 (top-center), an amplification of the MEP around the chlorine atom is provided. In both compounds the MEP surface and anisotropy at the Cl-atom are equivalent: +11.3 kcal mol^{-1} at the σ-hole and −3.7 kcal mol^{-1} at the negative belt.

In Fig. 6, we have represented two selected dimers of compounds **1** and **2**, where the Cl-atom is involved in halogen bonding interactions. In the case of compound **1**, the C–Cl bond points to the negative belt of the adjacent Cl-atom and in the

Fig. 5 MEP surfaces of compounds **1** (a) and **2** (b) and the RI-BP86-D3/def2-TZVP level of theory. Some MEP values are indicated in kcal mol^{-1}. An amplification of the MEP around the Cl-atom is also provided.
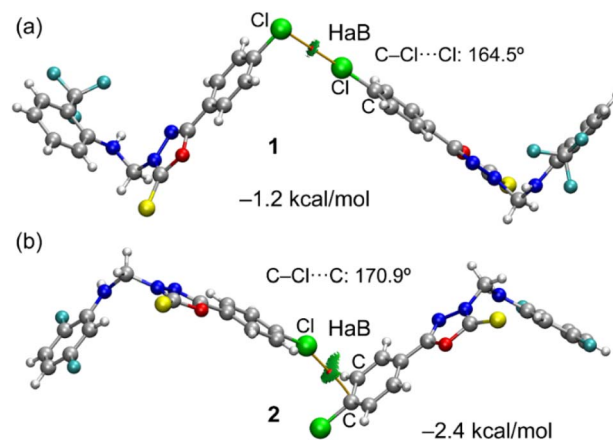
Fig. 6 QTAIM and NCIplot analyses of the HaB dimers observed in the X-ray structures of compounds **1** (a) and **2** (b). Only intermolecular bond CP (red spheres) and bond paths (orange lines) are represented. For the NCI plot settings, see computational methods.

case of compound **2**, to one C-atom of the aromatic ring. The dimerization energies are modest (-1.2 kcal mol^{-1} and -2.4 kcal mol^{-1}) but favourable in both cases. It should be emphasized that the MEP over the chlorophenyl ring is positive, thus indicating that in compound **2**, the halogen bond is likely not dominated by electrostatic effects and that other forces like dispersion or polarization likely compensate for the small electrostatic repulsion. The directionality of the HaB in compound **2** is better than in compound **1**, in line with the stronger interaction. Fig. 6 also shows the combined QTAIM and NCI plot analysis of both HaB dimers. The QTAIM analysis shows one bond critical point (CP, represented as a small red sphere) and the bond path (orange line) interconnecting both Cl-atoms in the dimer of **1**, thus confirming the existence of the HaB contact. Moreover, the interaction is further characterized by a green RDG isosurface coincident with the location of bond CP, which supports the attractive nature of the interaction. For compound **2**, the interaction is characterized a bond CP and a bond path connecting the Cl-atom to one C-atom of the aromatic ring. The NCIplot shows the presence of a green RDG isosurface that emerges upon dimerization and embraces one of the CC bonds of the aromatic ring, suggesting that both C-atoms are involved in the interaction, as further studied below.

To further investigate the halogen bonding nature of the contacts, especially in compound **2** where the MEP analysis suggests that the chlorophenyl π-system is electron deficient, we have used the electron localization function (ELF). This computational tool is useful to identify LPs and σ-holes.[57] The 2D ELF maps are represented in Fig. 7, where we have used the 2D plane defined by the atoms involved in the HaB (these atoms are also indicated in Fig. 6). It can be observed that in compound **1**, the σ-hole at the Cl-atom is pointing to the belt of the electron donor Cl-atom of the adjacent molecule, as expected for a true halogen bonding interaction. In fact, the bond path that connects both Cl-atoms crosses very close to the maximum electron depletion (σ-hole). For compound **2**, the σ-hole points to the π-system of the C=C bond, thus also confirming the HaB nature, in spite of the positive MEP.

3.7. Topological analysis of intermolecular interactions

To assess the nature and strength of the intermolecular interactions observed in various molecular dimers of **1** and **2**, we calculated the topological properties of these interactions mentioned in the experimental section. The molecular graphs of dimers show the bond critical points (BCPs) for the

intermolecular interactions illustrated in Fig. S6 and S7 (ESI†), and the topological parameters for the intermolecular interactions are summarized in Table S1 (ESI†). All the observed interactions are closed-shell interactions according to the value of $|-V(r)/G(r)| < 1$, $\nabla^2\rho(r) > 0$ and $H(r) > 1$.[58] In **1**, the dissociation energies (D_e) for two of the C–H⋯F interactions are relatively higher compared to other interactions observed. It is of interest to note that the dissociation energy of C16–F1⋯F2–C16 interaction is comparable to the strength of two of the C–H⋯F interactions. The experimental charge density values were reported for the F⋯F interactions with type I, type II and, quasi-I/II geometries.[59] The electron density ($\rho(r)$) is in the range of 0.02–0.07 e Å^{-3} and the Laplacian of the electron density ($\nabla^2\rho(r)$) falls in the range of 0.5–1.3 e Å^{-5}. In the present study, these values are comparable to experimental charge density values. We also noted that the strength of the C–Cl⋯Cl halogen bond and C⋯C and C–H⋯π, C–H⋯S, and one of the C–H⋯F interactions is relatively weaker than the F⋯F interaction.

In **2**, the strength of N–H⋯S ($D_e = 2.2$ kcal mol^{-1}) and one of the C–H⋯F interactions ($D_e = 2.1$ kcal mol^{-1}) is comparable, and they are relatively higher compared to other interactions. We also noted that the strength of a halogen bond (C–Cl⋯π) is comparable to that of C–H⋯N/F. The dissociation energy of the unconventional fluorine bond of type F1⋯O1 contact is the same as that of a Cl⋯π halogen bond and unconventional S⋯π contact. The intermolecular C–H⋯Cl interaction is relatively weaker than other interactions observed in **2**.

3.8. *In vitro* antimicrobial activity

The results of the initial antimicrobial screening of compounds **1** and **2** (200 μg/disc), the antibacterial antibiotics gentamicin sulfate, ampicillin trihydrate, and the antifungal drug clotrimazole (100 μg/disc) are outlined in Table 4. As evident from Table 4, compounds **1** and **2** showed marked antibacterial activity against all tested Gram-positive bacterial strains, marginal inhibitory activity against *Escherichia coli*, and lacked inhibitory activity against *Pseudomonas aeruginosa*. Compound
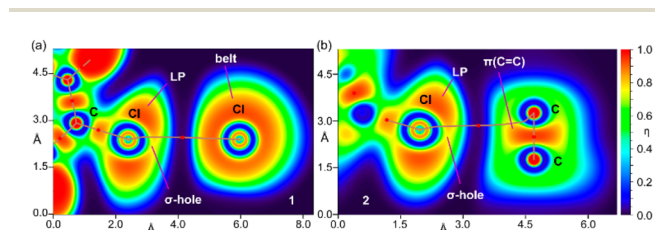
Fig. 7 2D maps of η(r) function for the dimers of **1** (a) and **2** (b). The molecular planes correspond to the C-atoms labelled in Fig. 1.

Table 4 Antimicrobial activity of compounds **1** and **2** (200 μg/8 mm disc), the broad spectrum antibacterial drugs gentamicin sulfate (100 μg/8 mm disc), ampicillin trihydrate (100 μg/8 mm disc) and the antifungal drug clotrimazole (100 μg/8 mm disc) against *Staphylococcus aureus* ATCC 6571 (*SA*), *Bacillus subtilis* ATCC 5256 (*BS*), *Micrococcus luteus* ATCC 27141 (*ML*), *Escherichia coli* ATCC 8726 (*EC*), *Pseudomonas aeruginosa* ATCC 27853 (*PA*), and the yeast-like pathogenic fungus *Candida albicans* MTCC 227 (*CA*)

Compound	Diameter of growth inhibition zone^a (mm)					
	SA	BS	ML	EC	PA	CA
1	21 (4)	18 (16)	16	12	—	11
2	22 (8)	24 (2)	18 (16)	11	—	—
Gentamicin sulfate	27 (1)	26 (2)	20 (2)	22 (0.5)	21 (0.5)	NT
Ampicillin trihydrate	22 (2)	23 (1)	20 (2)	16 (8)	18 (8)	NT
Clotrimazole	NT	NT	NT	NT	NT	21 (4)

^{a} Figures shown in parentheses represent the MIC values (μg mL^{-1}), NT: not tested, (—): inactive (inhibition zone < 10 mm.

1 displayed weak inhibitory activity against the pathogenic fungus *Candida albicans*, while compound **2** was totally inactive.

The minimal inhibitory concentration (MIC) of compounds **1** and **2** was assessed against the same microorganism used in the preliminary screening using the micro-dilution susceptibility method in Müller-Hinton Broth.[60] The values of the MIC for compounds **1**, **2** and the reference antimicrobial drugs gentamicin sulfate, ampicillin trihydrate, and clotrimazole (Table 4) were almost consistent with their growth inhibition zones.

3.9. *In vitro* anti-proliferative activity

The results of *in vitro* anti-proliferative activity of compounds **1** and **2** and the anticancer drug doxorubicin are shown in Table 5. The anti-proliferative activity outcomes showed that 2,5-difluorphenyl analogue **2** displayed marked anti-proliferative activity with $IC_{50} < 25$ μM against HepG-2 and MCF-7 cell lines and retained weak activity against PC-3 and HCT-116 cell lines. Meanwhile, the 2-(trifluoromethyl)phenyl analogue **1** displayed good anti-proliferative activity against HepG-2 and moderate activity against MCF-7 cell lines, and its activity against PC-3 and HCT-116 cell lines was almost similar to compound **1**.

3.10. Molecular docking analysis

In order to corroborate the experimental *in vitro* data, we performed a molecular docking simulation for four important drug targets, two of which are expressed in many tumor cells (human thymidine phosphorylase and human thymidylate synthase) and one target (thymidine phosphorylase) taken from the *E.coli* K12 strain and a drug target namely pyrimidine-nucleoside phosphorylase from *Staphylococcus aureus* strain COL was considered. The extra precision (XP) glide scoring scheme was used to predict the favourable pose at the protein active site and a score for the most favourable pose. Table 6 summarizes the glide XP docking scores for compounds **1** and **2** against these targets. For the control experiment, the co-crystallized ligand bound to these targets was docked and the score was compared with compounds **1** and **2**. The co-crystallized ligands showed a higher binding affinity in all four cases toward the respective target. However, compounds **1** and **2** also displayed a negative glide XP score, suggesting that they could also bind to the active

Table 6 Glide XP docking score expressed in kcal mol^{-1} for compounds **1** and **2** and co-crystallized ligand in the respective target

Compound code	Glide XP docking score
Human thymidine phosphorylase	
CMU	−11.578
1	−4.917
2	−6.748
***E.coli* K12 strain thymidine phosphorylase**	
0NP	−10.487
1	−6.987
2	−5.926
Human thymidylate synthase	
UFP	−9.271
1	−4.519
2	−4.024
***Staphylococcus aureus* strain COL pyrimidine-nucleoside phosphorylase**	
THM	−7.599
1	−3.812
2	−4.278

site of the respective target. The intermolecular interactions between compounds **1** and **2** and the critical active site residues in the respective protein targets are illustrated in Fig. 8.

In the human thymidine phosphorylase complex, the binding affinity of compound **2** is slightly better than compound **1**. An analysis of protein-ligand interaction reveals that in the human thymidine phosphorylase complex, residues Leu 148, Lys 157, Tyr 199, Ile 214, and Ile 218 establish hydrophobic interactions with the terminal aromatic rings of compound **1**. The amine group of **1** is involved in a hydrogen bond (N–H⋯O) with the backbone O atom of the Thr 118, and one of the F atoms of compound **1** has established a linear F⋯O contact (3.94 Å and 165°) with the backbone O atom of the Val 208. Compound **2** also establishes similar types of hydrophobic interactions with active site residues in human thymidine phosphorylase complex. Instead of an N–H⋯O hydrogen bond, an N–H⋯N hydrogen bond is formed between compound **2** and His 116. Similarly, instead of a linear F⋯O contact, an intermolecular F⋯N contact (3.14 Å, 156°) is formed between **2** and side chain N atom of the Lys 221 (Fig. 8a).

In the *E.coli* thymidine phosphorylase complex, compound **1** shows a slightly better affinity for the enzyme than compound **2**, as shown in Table 6. Fig. 8b shows different modes for compounds **1** and **2** at the active site, as seen from the interacting residues. We also see from this figure that compound **1** is slightly folded when it binds to the enzyme, whereas compound **2** exhibits a relatively extended conformation at the active site. The differences in affinity could be understood as the preferable binding conformations of these compounds. In addition to the hydrophobic interactions formed by residues Leu 117, Tyr 168, Ile 183, and Ile 187, a highly directional σ-hole (halogen bond) interaction is formed between the Cl atom of **1** and the O atom of the backbone Ser 113 (Cl⋯O = 3.68 Å, ∠C–Cl⋯O = 175°).

Table 5 *In vitro* anti-proliferative activity of compounds **1** and **2** and the anticancer drug doxorubicin towards hepatocellular carcinoma (HepG-2), human prostate cancer (PC-3), colorectal carcinoma (HCT-116) and mammary gland breast cancer (MCF-7) cell lines

Compound	IC_{50} (μM)^a			
	HepG-2	PC-3	HCT-116	MCF-7
1	**22.15 ± 1.5**	55.25 ± 3.2	48.28 ± 3.4	30.18 ± 2.6
2	**18.20 ± 1.1**	44.28 ± 2.6	52.60 ± 3.8	**24.04 ± 1.8**
Doxorubicin	4.50 ± 0.2	8.87 ± 0.6	5.23 ± 0.3	4.17 ± 0.2

^{a} IC_{50} values presented as the mean ± SD of three separate determinations.
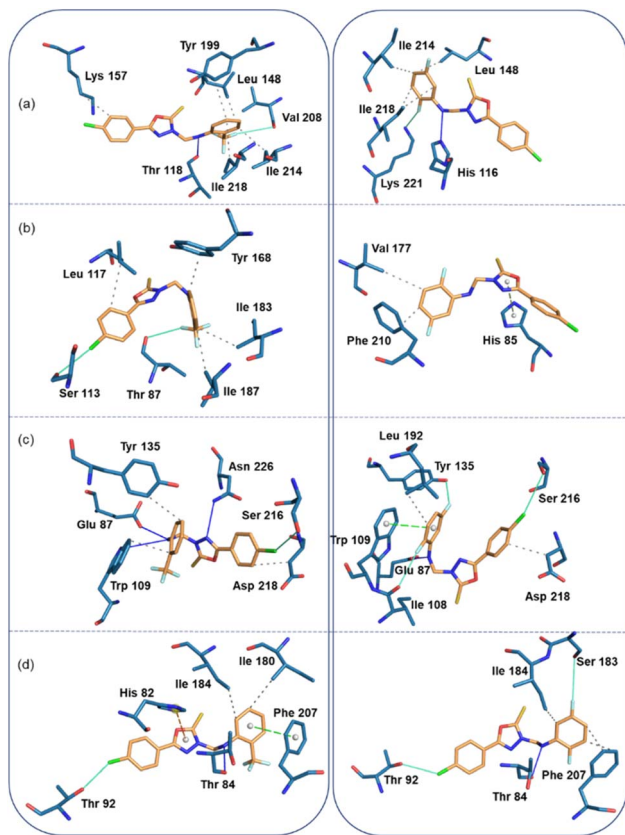
Fig. 8 Protein–ligand interactions (left panel: compound **1** and right panel: compound **2**). (a) Human thymidine phosphorylase, (b) *E. coli* thymidine phosphorylase, (c) Human thymidylate synthase, and (d) *S. aureus* pyrimidine-nucleoside phosphorylase.

One of the F atoms of **1** is involved in an interaction with the backbone O atom of Thr 87 residue (F···O = 3.17 Å, ∠C–F···O = 147°). The strong affinity could arise from forming halogen contacts between compound **1** and the active site residues. Unlike compound **1**, compound **2** establishes only two hydrophobic interactions with the active site residues Val 177 and Phe 210. In addition, the residue His 85 forms a π-stacking interaction (with a T-shaped configuration) with the oxadiazole ring.

In the thymidylate synthase complex, both compounds exhibit folded conformations at the active site and show comparable affinity towards the enzyme. As shown in Fig. 8c, compound **1** establishes three hydrogen bonds with the active site residues Glu 87, Trp 109, and Asn 226. In addition, the residues Trp 109, Tyr 135, and Asp 218 have hydrophobic interactions with compound **1**. There is a σ-hole interaction is formed between the Cl atom and the side chain O atom of Ser 216 (Cl···O = 3.44 Å, ∠C–Cl···O = 148°). The number of hydrogen bonds (Glu 87) and hydrophobic interactions (Leu 192 and Asp 218) is reduced in enzyme-compound **2** compared to the enzyme-compound **1** complex. However, three halogens (F and Cl) involved non-bonded interactions formed with the O atoms of the residues Ile 108, Tyr 135 and Ser 216 residues. The F···O (Ile 108) distance is 3.31 Å and ∠C–F···O = 162°. For another F···O (Tyr 135), separation is 2.90 Å and ∠C–F···O =

144°. The C–Cl···O (3.74 Å, 161°) halogen bond is highly directional and helps stabilize the complex.

In the *S. aureus* pyrimidine-nucleoside phosphorylase complex, both compounds show comparable affinity for the enzyme. Compound **1** establishes a hydrogen bonding interaction with the Thr 84 residue (Fig. 8d). The active site residues Ile 180 and 184 are involved in hydrophobic interactions. The active site residue Phe 207 stacks against ring C of compound **1** and His 82 establishes a cation-π interaction with the central oxadiazole ring. It is interesting to observe that the A ring of the Cl atom participates in the halogen bonding interaction with the Thr 92 residue (C–Cl···O = 3.4 Å, and ∠C–Cl···O = 153°). All these active site residues are involved in intermolecular interactions except for residues His 82 and Ile 180 in **2**. Ser 183 is in contact with one of the F atoms of the ring C. The distance between F and O is 3.9 Å and ∠C–F···O = 157°).

4. Conclusions

This effort involved the synthesis of two 3-arylaminomethyl *N*-Mannich bases and their structural characterization by a single-crystal X-ray diffraction approach. A thorough examination of the nature and strength of many types of intermolecular interactions, including hydrogen bonds, halogen bonding, unconventional F···O fluorine bond, and C–F···F–C contact. Further, the C–F···F–C contact exhibits a quasi-type I/II geometry. Based on the CSD analysis, the geometrical preference (type I) of C–F···F–C contact is quite comparable to the Cl···Cl contact. Moreover, the σ-hole on the Cl atom is revealed by the electrostatic potential map, and it functions as a donor for two distinct kinds of halogen bonds (Cl···Cl in compound **1** and Cl···π in compound **2**). The former contact exhibits L-shaped type II geometry, while the latter contact adopts type III linear geometry. Cl···π halogen bond-mediated dimer is two-fold stronger than one generated by a Cl···Cl halogen bond, according to dimerization energy calculations. Cooperativity with other interactions, such as C–H···S, N–H···S interactions, and unconventional F···O fluorine bond, is one of the common characteristics shared by C–H···F hydrogen bonds. Furthermore, the *in vitro* experiments showed that compounds **1** and **2** displayed antibacterial activity against all tested Gram-positive bacterial strains and marginal activity against *E. coli*. In addition, compound **1** showed weak inhibition activity against *Candida albicans*, while compound **2** was completely inactive. This result suggests the role of substituent groups, especially trifluorophenyl and di-substituted fluorophenyl, in the observed biological activity. We also showed that the title compounds had antiproliferative activities against different cancer cell lines. Molecular docking analysis indicated that both compounds could establish intermolecular interactions with active site residues of bacterial and cancer protein targets. We also noted that halogen atoms (Cl and F) are found to be involved in the intermolecular interactions with the active site residues, indicating that these halogens play a significant role in the observed bioactivity. Solid-state interactions and their strength and bioactivity help optimize the ligand molecules to

achieve better antibacterial and anticancer activity while retaining the triazole core.

Conflicts of interest

The authors declare that they have no competing interests.

Acknowledgements

References

1 (a) K. Rana and J. K. Sahu, *Curr. Drug Res. Rev.*, 2021, **13**, 90–100; (b) N. Desai, J. Monapara, A. Jethawa, V. Khedkar and B. Shingate, *Arch. Pharm.*, 2022, **355**, 2200123; (c) J.-J. Wang, W. Sun, W.-D. Jia, M. Bian and L.-J. Yu, *J. Enzyme Inhib. Med. Chem.*, 2022, **37**, 2304–2319.

2 M. Ogata, H. Atobe, H. Kushida and K. Yamamoto, *J. Antibiot.*, 1971, **24**, 443–451.

3 D. R. Shepard and R. Dreicer, *Expert Opin. Invest. Drugs*, 2010, **19**, 899–908.

4 K. C. Rees, Z. Dou and D. C. Whitehead, *ACS Infect. Dis.*, 2022, **8**, 911–917.

5 V. Summa, A. Petrocchi, F. Bonelli, B. Crescenzi, M. Donghi, M. Ferrara, F. Fiore, C. Gardelli, O. Gonzalez Paz, D. J. Hazuda, P. Jones, O. Kinzel, R. Laufer, E. Monteagudo, E. Muraglia, E. Nizi, F. Orvieto, P. Pace, G. Pescatore, R. Scarpelli, K. Stillmock, M. V Witmer and M. Rowley, *J. Med. Chem.*, 2008, **51**, 58435855.

6 (a) S. Bajaj, M. S. Kumar, H. Tinwala and M. YC, *Bioorg. Chem.*, 2021, **111**, 104873; (b) Z. M. M. Alzhrani, M. M. Alam, T. Neamatallah and S. Nazreen, *J. Enzyme Inhib. Med. Chem.*, 2020, **35**, 1116–1123; (c) S. A. Shahzad, M. Yar, M. Bajda, L. Shahzadi, Z. A. Khan, S. A. R. Naqvi, S. Mutahir, N. Mahmood and K. M. Khan, *Bioorg. Chem.*, 2015, **60**, 37–41.

7 M. M. Alam, S. Nazreen, A. S. A. Almalki, A. A. Elhenawy, N. I. Alsenani, S. E. I. Elbehairi, A. M. Malebari, M. Y. Alfaifi, M. A. Alsharif and S. Y. M. Alfaifi, *Pharmaceuticals*, 2021, **14**, 870.

8 M. Hagras, M. A. Saleh, R. R. Ezz Eldin, A. A. Abuelkhir, E. G. Khidr, A. A. El-Husseiny, H. A. El-Mahdy, E. B. Elkaeed and I. H. Eissa, *J. Enzyme Inhib. Med. Chem.*, 2022, **37**, 380–396.

9 (a) S. Valente, D. Trisciuoglio, T. De Luca, A. Nebbioso, D. Labella, A. Lenoci, C. Bigogno, G. Dondio, M. Miceli, G. Brosch, D. Del Bufalo, L. Altucci and A. Mai, *J. Med. Chem.*, 2014, **57**, 6259–6265; (b) V. R. Pidugu, N. S. Yarla,

A. Bishayee, A. M. Kalle and A. K. Satya, *Apoptosis*, 2017, **22**, 1394–1403.

10 M. C. Tuma, A. Malikzay, X. Ouyang, D. Surguladze, J. Fleming, S. Mitelman, M. Camara, B. Finnerty, J. Doody, E. L. P. Chekler, P. Kussie and J. R. Tonra, *Transl. Oncol.*, 2010, **3**, 318–325.

11 J. Sun, M.-H. Li, S.-S. Qian, F.-J. Guo, X.-F. Dang, X.-M. Wang, Y.-R. Xue and H.-L. Zhu, *Bioorg. Med. Chem. Lett.*, 2013, **23**, 2876–2879.

12 M. D. Altıntop, B. Sever, G. Akalın Çiftçi, G. Turan-Zitouni, Z. A. Kaplancıklı and A. Özdemir, *Eur. J. Med. Chem.*, 2018, **155**, 905–924.

13 (a) S. Bajaj, P. P. Roy and J. Singh, *Adv. Anticancer Agents Med. Chem.*, 2017, **17**, 1869–1883; (b) J. Sun, H. Zhu, Z.-M. Yang and H.-L. Zhu, *Eur. J. Med. Chem.*, 2013, **60**, 23–28.

14 C. D. Mohan, N. C. Anilkumar, S. Rangappa, M. K. Shanmugam, S. Mishra, A. Chinnathambi, S. A. Alharbi, A. Bhattacharjee, G. Sethi, A. P. Kumar, Basappa and K. S. Rangappa, *Front. Oncol.*, 2018, **8**, 42.

15 E. Mitsiki, A. C. Papageorgiou, S. Iyer, N. Thiyagarajan, S. H. Prior, D. Sleep, C. Finnis and K. R. Acharya, *Biochem. Biophys. Res. Commun.*, 2009, **386**, 666–670.

16 (a) Y.-Y. Wu, W.-B. Shao, J.-J. Zhu, Z.-Q. Long, L.-W. Liu, P.-Y. Wang, Z. Li and S. Yang, *J. Agric. Food Chem.*, 2019, **67**, 13892–13903; (b) Z. Yang, Y. Sun, Q. Liu, A. Li, W. Wang and W. Gu, *J. Agric. Food Chem.*, 2021, **69**, 13373–13385.

17 (a) M. Inoue, Y. Sumii and N. Shibata, *ACS Omega*, 2020, **5**, 10633–10640; (b) J. Han, L. Kiss, H. Mei, A. M. Remete, M. Ponikvar-Svet, D. M. Sedgwick, R. Roman, S. Fustero, H. Moriwaki and V. A. Soloshonok, *Chem. Rev.*, 2021, **121**, 4678–4742; (c) J. He, Z. Li, G. Dhawan, W. Zhang, A. E. Sorochinsky, G. Butler, V. A. Soloshonok and J. Han, *Chinese Chem. Lett.*, 2023, **34**, 107578.

18 (a) L. H. Al-Wahaibi, A. A. B. Mohamed, S. S. Tawfik, H. M. Hassan and A. A. El-Emam, *Molecules*, 2021, **26**, 2110; (b) A. A. El-Emam, O. A. Al-Deeb, M. Al-Omar and J. Lehmann, *Bioorg. Med. Chem.*, 2004, **12**, 5107–5113.

19 (a) L. H. Al-Wahaibi, A. Alsfouk, A. A. El-Emam and O. Blacque, *Acta Crystallogr., Sect. E: Crystallogr. Commun.*, 2019, **75**, 611–615; (b) L. H. Al-Wahaibi, N. S. Kumar, A. A. El-Emam, N. S. Venkataramanan, H. A. Ghabbour, A.-M. S. Al-Tamimi, J. Percino and S. Thamotharan, *J. Mol. Struct.*, 2019, **1175**, 230–240.

20 L. Ma, Y. Xiao, C. Li, Z.-L. Xie, D.-D. Li, Y.-T. Wang, H.-T. Ma, H.-L. Zhu, M.-H. Wang and Y.-H. Ye, *Bioorg. Med. Chem.*, 2013, **21**, 6763–6770.

21 (a) A.-M. S. Al-Tamimi, O. A. Al-Deeb, A. A. El-Emam, S. W. Ng and E. R. T. Tiekink, *Acta Crystallogr., Sect. E: Struct. Rep. Online*, 2013, **69**, o729; (b) A.-M. S. Al-Tamimi, A. M. Alafeefy, A. A. El-Emam, S. W. Ng and E. R. T. Tiekink, *Acta Crystallogr., Sect. E: Struct. Rep. Online*, 2013, **69**, o730; (c) M. A. Al-Alshaikh, H. A. Ghabbour, A.-M. S. Al-Tamimi, M. S. M. Abdelbaky, S. Garcia-Granda and A. A. El-Emam, *Z. Kristallogr.–New Cryst. Struct.*, 2016, **231**, 301–303; (d) R. I. Al-Wabli, N. A. El-Emam, H. A. Ghabbour, N. G. Haress and A. A. El-

Emam, *Z. Kristallogr.–New Cryst. Struct.*, 2016, **231**, 815–817; (*e*) L. H. Al-Wahaibi, H. A. Ghabbour, F. A. M. Al-Omary, E. R. T. Tiekink and A. A. El-Emam, *Z. Kristallogr.–New Cryst. Struct.*, 2022, **237**, 587–591.

22 (*a*) T. Steiner, *Angew. Chem., Int. Ed.*, 2002, **41**, 48–76; (*b*) G. R. Desiraju, *Chem. Commun.*, 2005, **2005**, 2995–3001; (*c*) G. Bulusu and G. R. Desiraju, *J. Indian Inst. Sci.*, 2020, **100**, 31–41.

23 Z. S. Derewenda, *Int. J. Mol. Sci.*, 2023, **24**, 13165.

24 (*a*) C. B. Aakeroy, D. L. Bryce, G. R. Desiraju, A. Frontera, A. C. Legon, F. Nicotra, K. Rissanen, S. Scheiner, G. Terraneo, P. Metrangolo and G. Resnati, *Pure Appl. Chem.*, 2019, **91**, 1889–1892; (*b*) G. R. Desiraju, P. S. Ho, L. Kloo, A. C. Legon, R. Marquardt, P. Metrangolo, P. Politzer, G. Resnati and K. Rissanen, *Pure Appl. Chem.*, 2013, **85**, 1711–1713; (*c*) A. Varadwaj, P. R. Varadwaj, H. M. Marques and K. Yamashita, *Inorganics*, 2022, **10**, 149; (*d*) P. R. Varadwaj, A. Varadwaj, H. M. Marques and K. Yamashita, *CrystEngComm*, 2023, **25**, 1411–1423.

25 (*a*) J. Badorrek and M. Walter, *J. Comput. Chem.*, 2022, **43**, 340–348; (*b*) M. Hajji, N. Abad, M. A. Habib, S. M. H. Elmgirhi and T. Guerfel, *J. Indian Chem. Soc.*, 2021, **98**, 100208; (*c*) M. Hajji, H. Mtiraoui, N. Amiri, M. Msaddek and T. Guerfel, *Int. J. Quantum Chem.*, 2019, **119**, e26000.

26 R. C. Clark and J. S. Reid, *Acta Crystallogr., Sect. A: Found. Crystallogr.*, 1995, **51**, 887–897.

27 O. V Dolomanov, L. J. Bourhis, R. J. Gildea, J. A. K. Howard and H. Puschmann, *J. Appl. Crystallogr.*, 2009, **42**, 339–341.

28 G. Sheldrick, *Acta Crystallogr., Sect. A: Found. Crystallogr.*, 2015, **71**, 3–8.

29 G. Sheldrick, *Acta Crystallogr., Sect. C: Cryst. Struct. Commun.*, 2015, **71**, 3–8.

30 A. Spek, *Acta Crystallogr., Sect. D: Biol. Crystallogr.*, 2009, **65**, 148–155.

31 C. F. Macrae, I. Sovago, S. J. Cottrell, P. T. A. Galek, P. McCabe, E. Pidcock, M. Platings, G. P. Shields, J. S. Stevens, M. Towler and P. A. Wood, *J. Appl. Crystallogr.*, 2020, **53**, 226–235.

32 M. A. Spackman and D. Jayatilaka, *CrystEngComm*, 2009, **11**, 19–32.

33 M. A. Spackman and J. J. McKinnon, *CrystEngComm*, 2002, **4**, 378–392.

34 M. J. Turner, J. J. McKinnon, S. K. Wolff, D. J. Grimwood, P. R. Spackman, D. Jayatilaka and M. A. Spackman, 2017.

35 R. Ahlrichs, M. Bär, M. Häser, H. Horn and C. Kölmel, *Chem. Phys. Lett.*, 1989, **162**, 165–169.

36 (*a*) A. D. Becke, *J. Chem. Phys.*, 1997, **107**, 8554–8560; (*b*) H. L. Schmider and A. D. Becke, *J. Chem. Phys.*, 1998, **108**, 9624–9631; (*c*) S. Grimme, J. Antony, S. Ehrlich and H. Krieg, *J. Chem. Phys.*, 2010, **132**, 154104.

37 R. F. W. Bader, *Chem. Rev.*, 1991, **91**, 893–928.

38 J. Contreras-García, E. R. Johnson, S. Keinan, R. Chaudret, J.-P. Piquemal, D. N. Beratan and W. Yang, *J. Chem. Theory Comput.*, 2011, **7**, 625–632.

39 W. Humphrey, A. Dalke and K. Schulten, *J. Mol. Graph.*, 1996, **14**(27–28), 33–38.

40 A. D. Becke and K. E. Edgecombe, *J. Chem. Phys.*, 1990, **92**, 5397–5403.

41 T. Lu and F. Chen, *J. Comput. Chem.*, 2012, **33**, 580–592.

42 G. L. Woods and J. A. Washington, Antibacterial susceptibility tests: dilution and disk diffusion methods, in *Manual of Clinical Microbiology*, ed. P. R. Murray, E. J. Baron, M. A. Pfaller, F. C. Tenover and R. H. Yolken, American Society of Microbiology, Washington, DC, USA, 1995.

43 I. Wiegand, K. Hilpert and R. E. Hancock, *Nat. Protoc.*, 2008, **3**, 163–175.

44 T. Mosmann, *J. Immunol. Methods*, 1983, **65**, 55–63.

45 R. A. Norman, S. T. Barry, M. Bate, J. Breed, J. G. Colls, R. J. Ernill, R. W. A. Luke, C. A. Minshull, M. S. B. McAlister, E. J. McCall, H. H. J. McMiken, D. S. Paterson, D. Timms, J. A. Tucker and R. A. Pauptit, *Structure*, 2004, **12**, 75–84.

46 C. Pozzi, S. Ferrari, R. Luciani, G. Tassone, M. P. Costi and S. Mangani, *Molecules*, 2019, **24**, 1257.

47 C. Lu, C. Wu, D. Ghoreishi, W. Chen, L. Wang, W. Damm, G. A. Ross, M. K. Dahlgren, E. Russell, C. D. Von Bargen, R. Abel, R. A. Friesner and E. D. Harder, *J. Chem. Theory Comput.*, 2021, **17**, 4291–4300.

48 R. A. Friesner, R. B. Murphy, M. P. Repasky, L. L. Frye, J. R. Greenwood, T. A. Halgren, P. C. Sanschagrin and D. T. Mainz, *J. Med. Chem.*, 2006, **49**, 6177–6196.

49 M. F. Adasme, K. L. Linnemann, S. N. Bolz, F. Kaiser, S. Salentin, V. J. Haupt and M. Schroeder, *Nucleic Acids Res.*, 2021, **49**, W530–W534.

50 I. Saraogi, B. H. M. Mruthyunjayaswamy, O. B. Ijare, Y. Jadegoud and T. N. Guru Row, *Acta Crystallogr., Sect. E: Struct. Rep. Online*, 2002, **58**, o1341–o1342.

51 I. J. Bruno, J. C. Cole, M. Kessler, J. Luo, W. D. S. Motherwell, L. H. Purkis, B. R. Smith, R. Taylor, R. I. Cooper, S. E. Harris and A. G. Orpen, *J. Chem. Inf. Comput. Sci.*, 2004, **44**, 2133–2144.

52 L. H. Al-Wahaibi, B. Rahul, A. A. B. Mohamed, M. S. M. Abdelbaky, S. Garcia-Granda, A. A. El-Emam, M. J. Percino and S. Thamotharan, *ACS Omega*, 2021, **6**, 6996–7007.

53 P. R. Varadwaj, A. Varadwaj and H. M. Marques, *Crystals*, 2020, **10**, 146.

54 (*a*) M. Hajji, J. S. Al-Otaibi, M. Belkhiria, S. Dhifaoui, M. A. Habib, S. M. H. Elmgirhi, H. Mtiraoui, R. Bel-Hadj-Tahar, M. Msaddek and T. Guerfel, *J. Mol. Struct.*, 2021, **1223**, 128998; (*b*) M. J. Calhorda, *Chem. Commun.*, 2000, 801–809; (*c*) M. Hajji, A. Haouas, N. Abad and T. Guerfel, *ChemistrySelect*, 2023, **8**, e202302624.

55 M. A. A. Ibrahim, R. R. A. Saeed, M. N. I. Shehata, M. N. Ahmed, A. M. Shawky, M. M. Khowdiary, E. B. Elkaeed, M. E. S. Soliman and N. A. M. Moussa, *Int. J. Mol. Sci.*, 2022, **23**, 3114.

56 S. Tothadi, S. Joseph and G. R. Desiraju, *Cryst. Growth Des.*, 2013, **13**, 3242–3254.

57 D. F. Mertsalov, R. M. Gomila, V. P. Zaytsev, M. S. Grigoriev, E. V Nikitina, F. I. Zubkov and A. Frontera, *Crystals*, 2021, **11**, 1406.

58 C. Gatti, *Z. Kristallogr. - Cryst. Mater.*, 2005, **220**, 399–457.

59 (*a*) L. Singla, A. Kumar, C. M. Robertson, P. Munshi and A. Roy Choudhury, *Cryst. Growth Des.*, 2023, **23**, 853–861; (*b*) D. Chopra, T. S. Cameron, J. D. Ferrara and T. N. Guru Row, *J. Phys. Chem. A*, 2006, **110**, 10465–10477; (*c*) V. R. Hathwar and T. N. Guru Row, *Cryst. Growth Des.*, 2011, **11**, 1338–1346; (*d*) M. S. Pavan, K. Durga Prasad and T. N. Guru Row, *Chem. Commun.*, 2013, **49**, 7558–7560; (*e*) D. E. Hibbs, J. Overgaard, J. A. Platts, M. P. Waller and M. B. Hursthouse, *J. Phys. Chem. B*, 2004, **108**, 3663–3672.

60 I. Wiegand, K. Hilpert and R. E. W. Hancock, *Nat. Protoc.*, 2008, **3**, 163–175.